Using Support Vector Machine (SVM) and Ionospheric Total Electron Content (TEC) Data for Solar Flare Predictions

Saed Asaly, Lee-Ad Gottlieb, and Yuval Reuveni

***Abstract*—Predicting where and when space weather events such as solar flares and X-rays bursts are likely to occur in a specific area of interest constitutes a significant challenge in space weather research. Space weather scientists are, therefore, gradually exploring multivariate data analysis techniques from the fields of data mining or machine learning in order to approximate future occurrences of space weather events from past distribution patterns. As solar flares emit extreme ultraviolet and X-ray radiation, which leads to ionization effect in different layers of the ionosphere, most recent works related to solar flare predictions using machine learning (ML) techniques, focused on X-ray time series predictions. Here, we suggest using support vector machine for classifying subdaily and diurnal total electron content (TEC) spatial changes prior to solar flare events, in order to assess the possibility of predicting B, C, M, and X-class solar flare events. This is done as opposed to predicting TEC time series using ML techniques. The predictions are estimated up to three days before each tested class events, along with different skill scores such as precision, recall, Heidke skill score (HSS), accuracy, and true skill statistics. The results indicate that the suggested approach has the ability to predict solar flare events of X and M-class 24 h prior to their occurrence with 91% and 76% HSS skill scores, respectively, which improves over most recent related works. However, for the small-size C and B-class flares, the suggested approach does not succeed in producing similar promising results.**

***Index Terms*—Ionospheric total electron content, machine learning (ML), solar flare predictions, space weather, support vector machine (SVM).**

I. Introduction

A. Space Weather

SPACE weather is a field of research, which provides new perspectives into the complex interactions and effects of the sun and other cosmic sources on the earth's magnetosphere, ionosphere, and thermosphere, as well as on interplanetary space. Space weather also influences ground- and space-based technological systems and can also compromise human lives and health. Hence, space weather is a highly relevant research topic for our modern society. The effects of solar activity on earth and in space, such as satellite damage, radiation hazards to astronauts and airline passengers, telecommunication disturbances, and outages of electric power grids, have been well documented and studied in the last few decades [1]–[3]. Scientists are, therefore, pursuing reliable tools and methods for predicting where and when space weather events such as solar flares and X-rays bursts are likely to occur [4], [5]. The sun-earth system is a highly complex system with numerous physical processes, ranging from magnetic field reconnection and plasma acceleration processes [6], to the effects of charged particles on electronic and biological systems [7], covering a large range of spatial and temporal scales [8]. Although our understanding of the governing physics of the sun-earth system is constantly improving, the task of achieving real-time space weather forecasts, similar to the daily atmospheric weather forecasts, still remains a challenging task [7], [9] as our modern technologies and space infrastructures continue to be exposed to space weather threats.

Zhelavskaya *et al.* [10] tested how different machine learning (ML) techniques perform with nowcasting and forecasting Kp index up to 12 h ahead. Balasis *et al.* [11] utilized fuzzy artificial neural networks in order to detect ultralow frequency waves from magnetic field time series measurements using the CHAMP low earth orbit satellite. Others used ML approach applied with a data-driven model for the differential electron flux, with energies between 120–600 keV, in the outer radiation belt [12].

B. Solar Flares

Solar flares are huge outbursts of electromagnetic radiation from the sun with time scales ranging from minutes to hours [13]. The abrupt eruption of electromagnetic radiation propagates at the speed of light, hence, any outcome reflected on the sunlit side of earth's unprotected external atmosphere strikes simultaneously when the event is detected. The amplified level of extreme ultraviolet (EUV) and X-ray radiation leads to ionization effect in the ionospheric D, E, and F2 layers upon the sunlit side of earth [14].

Solar flare magnitudes cover a broad range of intensities and are categorized in terms of peak emission in the $0.1 - 0.8$ nm

Manuscript received August 11, 2020; revised November 27, 2020; accepted December 9, 2020. Date of publication December 14, 2020; date of current version January 8, 2021. This work was supported in part by the Israeli Ministry of Science, Technology and Space under Grant 3-14 517 and Grant 3-15 743, and in part by the Israel Science foundation under Grant 1602/19. *(Corresponding author: Yuval Reuveni.)*

Saed Asaly and Lee-Ad Gottlieb are with the Department of Computer Sciences, Ariel University, Ariel 40700, Israel (e-mail: saed.asaly@gmail.com; leead@ariel.ac.il).

Yuval Reuveni is with the Department of Physics, Ariel University, Ariel 40700, Israel, Eastern R&D center, Ariel 40700, Israel, and also with the School of Sustainability, Interdisciplinary Center Herzliya, Herzliya 4610101, Israel (e-mail: yuvalr@ariel.ac.il).

Digital Object Identifier 10.1109/JSTARS.2020.3044470

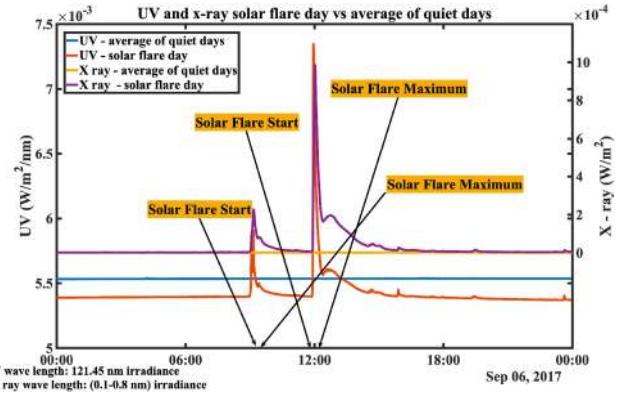

Fig. 1. UV and X-ray time series during a day (September 6, 2017) having two X-class solar flare occurred at 08:57, and 11:53 UTC, respectively, versus the averaged quiet DOY between the years 2010–2019.

spectral band (soft X-rays) of the NOAA/GOES XRS [15], [16]. The X-ray energy flux levels range from the "A" level (nominally starting at 10^{-8} W/m^2), followed by the next level, which is ten times stronger, "B" level flares ($\geq 10^{-7}$ W/m^2), "C" level flares (10^{-6} W/m^2), "M" level flares (10^{-5} W/m^2), extending up to "X" level flares (10^{-4} W/m^2).

Typically, high frequency (HF) radio waves are capable of supporting communication over large spatial scales by refraction throughout the ionospheric upper layers [14], [17]. When a strong solar flare strikes, it produces ionization in the lower layers of the ionosphere (mainly the D-layer), causing radio waves, which interact with electrons in these layers, to lose energy due to higher collision frequency that occurs in the higher density environment of the D-layer, thus causing HF radio signals to become attenuated or completely absorbed [18]. This may lead to an HF communication deficiency (i.e., radio blackout), mainly impacting the 3 to 30 MHz frequency band [19].

Solar flares typically develop in areas on the sun associated with the increase of strong magnetic fields [20], frequently coupled with sunspot groups active regions [21]. As these magnetic fields develop, they can extend to a state of instability while releasing energy in numerous forms [22]. These encompass also electromagnetic waves, which are detected as solar flares [15].

Nevertheless, the effect on the ionospheric F2 layer is induced by the EUV radiation, thus, if we examine the time series of both X-ray and EUV radiation during solar flare event, both peaks at the same time, hence providing the motivation to examine also the impact on the total electron content (TEC) in the ionosphere, which is mainly influenced by the F2 layer [23]. Fig. 1 shows a time series of both EUV and X-ray during two X-class solar flares events occurred in September 6, 2017; one starts at 08:57 UTC, and the other starts at 11:53 UTC, indicating a detectable signatures, versus the time series of an averaged EUV and X-ray measurements during the same day for years without solar flares occurrence. Zheng *et al.* [24] proposed a hybrid convolutional neural network model by modifying a variant of VGGNet (neural network, which performed very well in the ImageNet Large Scale Visual Recognition Challenge in 2014), to predict multi-class solar flare occurrence within 24 h by collecting samples of solar active regions data from 2010 May to 2018 September. Liu *et al.* [25], on the other hand, used physical parameters provided by the space-weather helioseismic and magnetic imager (HMI) active region patches along with other related data products such as survey X-ray flares occurred from May 2010 to December 2016. They managed to categorize their source regions into the four classes (B, C, M, and X) according to the maximum GOES magnitude of flares they generated, while using a random forest (RF) algorithm, to predict the occurrence of a certain flare class at a given active region within 24 h time frame [25]. Colak *et al.* applied image processing techniques in order to train two neural networks (NN) in which the first one used a numerical representation for the three parts of the McIntosh classification for the sunspot region, taking into account the sunspot area as inputs, and then generated the probability that this sunspot region will produce a C, M, or X class solar flare in the upcoming 24 h. The second NN was trained using a new dataset containing only the sunspot groups, which were associated with C, M, and X class flares [26].

Jiao *et al.* [27] developed a mixed LSTM regression model to predict the maximum solar flare intensity within a 24-h time window 0–24, 6–30, 12–36, and 24–48 h ahead of time using 6, 12, 24, and 48 h of data for each HMI active region patch.

C. Ionospheric TEC

One TEC unit (TECU) is defined as the total number of free electrons in a cylinder with a base area of 1 m^2, which is equal to 10^{16} electrons/m^2. The ionosphere structure and electron peak density varies markedly with altitude, latitude, longitude, universal time, season, solar cycle, and certain solar and geomagnetic activity, causing it to be dynamically variable, and hence, one of the main sources of errors to technology such as Global Positioning System (GPS) [28], [29]. The primary driving mechanism for the ionosphere is solar ultraviolet (UV) and extreme UV (EUV) radiation, which affect ionization, temperatures, and neutral winds [30], [31]. The study of ionospheric modulation due to solar events is a fundamental part of space weather research [23]. The strongest reaction of the ionosphere occurs during the complex coupling processes while geomagnetic storms associated with solar coronal mass ejections, coronal holes, or solar flares, with the impact observed at different heights in the ionosphere [13].

Global navigation satellite system (GNSS) technology is a powerful tool for space weather monitoring and forecast, which requires a permanent monitoring of the ionospheric state on a global scale [32]. The world-wide use of GNSS such as GPS and GLONASS enables an exceptional method for continuous monitoring of TEC of the global ionosphere/plasmasphere stretching up to a height of about 20 000 km [33]. The basic concept upon which these systems operate is accurately estimating the travel time of the electromagnetic signal emitted from satellites high above the earth's surface [34]. Since these signals must propagate through the earth's troposphere and the ionosphere, they are considerably affected by the physical characteristics of these layers. When electromagnetic signals propagate through the troposphere they are delayed, and the speed of propagation is decreased [35]. The amount of delay depends mainly on

the pressure, temperature and water vapor content, which vary significantly both in space and time [36]. Opposed to the nondispersive tropospheric effects, the speed at which electromagnetic waves travel at a specific height in the ionosphere is bounded by the local free electrons density [37], and the speed of the wave is actually increased by the presence of the free electrons. The outcome is that the electromagnetic wave phase accelerates as it propagates through the medium, causing it to arrive at the receiver earlier than it would have arrived had it traveled in a complete vacuum [38]. The early arrival is generally described as a phase advance. The total zenith ionospheric range error on a radio wave is estimated by integrating the free electron density along the total path from the satellite to the receiver, and thus is proportional to the TEC in the ionosphere [38].

Most of the effort invested so far in the field of ML related to TEC measurements were concentrated in TEC time series prediction algorithms. Sun *et al.* [39] provided a long short-term memory (LSTM) based model to predict ionospheric vertical TEC above Beijing, where their model input was a time sequence consisted of the daily TEC vectors and other closely related parameters, and the output were TEC time series 24 h ahead. Liu *et al.* [40], however, applied the LSTM with multiple input data, including historical time series of spherical harmonic (SH) coefficients, solar EUV flux, disturbance storm time index, and hour of the day, to forecast the 256 SH coefficients, which are traditionally used to construct global ionospheric maps. Thus, this is the first time an attempt has been carried out for using support vector machine (SVM) technique for classifying spatial TEC changes caused during solar flare events.

II. Motivation

Space weather research studies the interactions of the solar-terrestrial environment, which is drawing a significant scientific attention due to our increasing use of the space environment for satellites, GPS navigation, TV, and cell phone communication [5]. Extreme space weather could potentially cause damage to critical infrastructure, especially the electric grid, or the performance of technology we use on earth [41]. Current remote sensing technologies, operating at a wide range of electromagnetic spectrum, have become invaluable tools to detect and measure signatures associated with space weather events [42]. Although state-of-the-art forecasting systems today are based on numerical models, which describe the physical processes leading to space weather events, the lack of sufficiently detailed and real-time measurements prevents accurate forecasting of such events [43]. Predicting where and when a severe space weather events are likely to occur in a specific region of interest still remains a key challenge in severe space weather forecasting and mitigation [44].

Recent advances in cloud-based big-data technologies currently make data driven solutions feasible for increasing numbers of scientific computing applications [45], [46]. One such data driven solution approach is ML, where patterns in large datasets are brought to the surface by finding complex mathematical relationships within the data [47]. Researchers are, therefore, gradually exploring multivariate data analysis techniques from the field of ML in order to approximate future occurrences of space weather events from past distribution patterns [48]. Current studies have clarified patterns of spatial sensitivity, however temporal forecasts have remained largely empirical [49], [50]. Most ML techniques achieve overall success rates of $75\% - 95\%$ [51]. While this may seem very promising, there are issues which remain with data input quality, potential over fitting and inadequate choice of prediction models, introducing unintentional inclusion of redundant or noise variables, and technical limits to predicting only certain types and sizes of the flare event [52]–[54]. Simpler models provide only slightly inferior predictions to more complex models and should guide the way for a more widespread application of data mining in solar flares prediction [55], [56]. Here, we propose to study how to implement machine learning methods, such as SVMs, with global GPS-TEC dataset, constructed from ground base measurements, in order to forecast solar flare events.

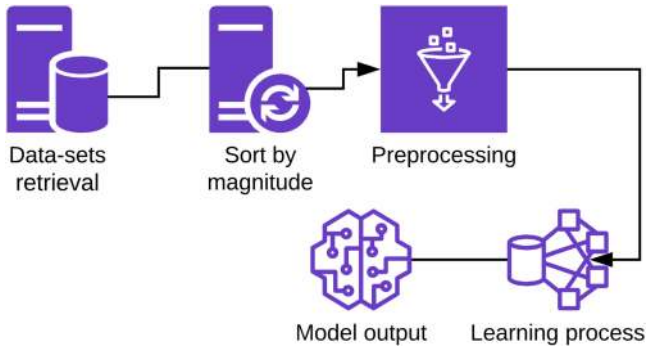

Fig. 2. Flowchart describing the steps of the proposed methodology. The suggested approach is consisted of the datasets retrieval, followed by datasets sorting by magnitudes. Furthermore, in order to optimize and accelerate the learning process, Preprocessing techniques were applied with the GPS-TEC data prior to the learning process.

The current suggested methodology is to utilize the SVM classification algorithm in order to predict solar flare events by applying it with spatial changes introduced into global TEC maps one, two, or three days before B, C, M, or X class solar flare.

III. Datasets and Methodology

Although severe space weather events are not common, low-level space weather events occur on a regular basis. Since the beginning of the 20th century, all aspects of our space-based technology have been affected by severe and extreme space weather disturbances. When they do occur, the impacts to our national infrastructures are extremely significant and the ability to predict them is of the highest priority in natural hazards prediction. Therefore, a considerable amount of efforts has been devoted for conducting continuous monitoring of different solar indices [30], augmenting current available datasets [57]. The workflow (shown in Fig. 2) of the suggested methodology consists of the dataset collection and preprocessing (averaging, differentiating), followed by the implementation of the SVM under various measures.

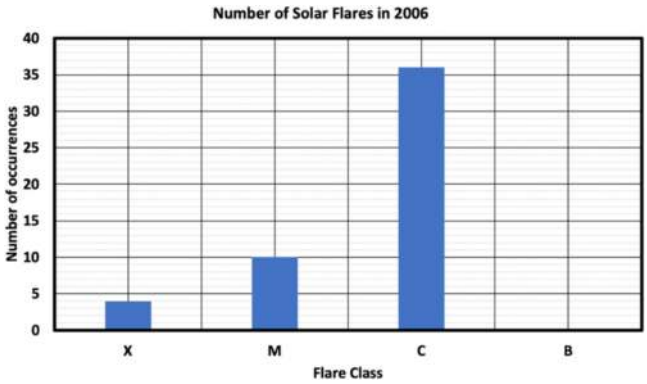

Fig. 3. Example for the sorting procedure step, applied with the strongest solar flare data available for the year 2006 [taken from https://spaceweatherlive.com]. As can be noticed, during the year 2006 only X, M, and C flare classes were registered among the strongest 50 solar flares, where there were 4 X-class solar flares, 10 M-class solar flares, and 36 B-class solar flares.

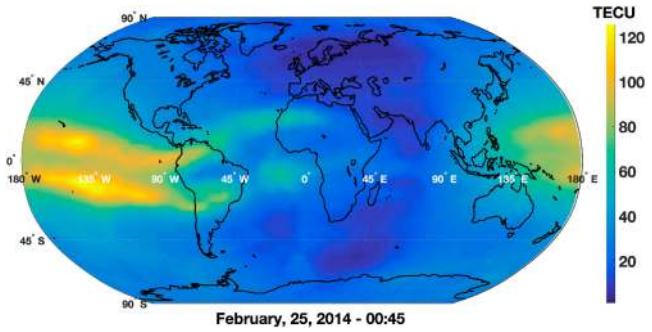

Fig. 4. Example of a global TEC map around the time of an X-class solar flare event, occurred on February 25, 2014, at 00:45 UTC. [source: ftp://cddis.nasa.gov/gnss/products/ionex/].

1) Solar Flares Dataset: For the solar flares dataset, we used the NOAA SWPC - spaceweatherlive.com website, which provides real-time auroral and solar activity and archive data since June 1996, based on the space environment monitor instrument subsystem, carried on board Geostationary Operational Environmental Satellites (GOES) [58]. The dataset consists of the strongest 50 solar flares each year, where for each flare the exact level, region, and time is provided. Since our primary goal is to study how ML methods can be implemented with GPS-TEC estimations to forecasts solar flare events, we examine only the solar flare events, which were timely correlated with the available GPS-TEC data between the years 1998–2018 (i.e., TEC data for the day of the flare and the three consecutive days before). After sorting the entire database, we arrived at 171 X-class solar flares, as well as 586 M-class, 193 C-class, and 100 B-class solar flare. A typical example for the sorting procedure, applied with the strongest solar flare data found for the year 2006 is shown in Fig. 3.

2) TEC Dataset: For each of the maps, we used the global ionospheric maps of VTEC computed with a resolution of 15 min, 5° and 2.5° in time, longitude and latitude, respectively, which results in 96 maps per day with dimension of 73×71 for each map [59]. A typical example of a VTEC map snapshot is shown in Fig. 4, corresponding to a X-class solar flare event.

3) TEC Dataset Selection: Due to the fact that there are five different models (CODE - University of Bern in Switzerland, ESA - ESOC Darmstadt Germany, JPL - Jet Propulsion Lab in Pasadena USA, and UPC -University Polytechnic Catalonia in Barcelona, Spain), which produces global ionospheric GPS-TEC maps, in addition to the International GNSS Service (IGS) Analysis Centre dataset, which contains also global ionospheric TEC maps, extracted from averaging the four different models, we first set to examine the differences between all 5 datasets, during quiet and disturbed days, to determine whether our learning results will be effected while using a specific model. The IGS dataset includes rapid global TEC maps and movies in cylindrical projection; rapid RMS TEC maps and errors of in cylindrical projection; and rapid TEC maps and movies in polar projection (https://spdf.gsfc.nasa.gov/pub/data/gps/tec15min_igs/).

Furthermore, following Liu *et al.* [60], which analyzed 11 years of global TEC maps, derived from the JPL model, while investigating a new approach for extracting overall climatological feature of the ionosphere, we divided each hemisphere into three separate strips: low, mid, and high latitude. The low strip ranges from latitudes $0^\circ - 25^\circ$, middle strips range from latitudes $25^\circ - 55^\circ$, and high strips ranges from latitudes $55^\circ - 87.5^\circ$. For each longitude, in each strip we calculated the mean TEC value, and as a result, we obtained for each individual longitude a single mean TEC value. In addition, as suggested by Liu *et al.* [60], we have also combined each strip with its identical one in both hemispheres, resulting in global low latitudes ($25^\circ N - 25^\circ S$) strip, global middle latitudes strip ($25^\circ N - 55^\circ N, 25^\circ S - 55^\circ S$), and global high latitudes strip ($55^\circ N - 87.5^\circ N, 55^\circ S - 87.5^\circ S$). This is done due to the fact that there is a strong solar activity variation in the daily global mean TEC strips [60], where the mean TEC indicates stronger solar activity sensitivity in the lower latitude strips, thus, the resulting saturation in the mean TEC versus F10.7 solar index is more prominent at low latitudes, however, the mean TEC increases more rapidly with higher solar EUV fluxes, evidently observed at high latitudes.

Fig. 5 shows the comparison between the three global strips (low, middle, and high latitudes) for each model versus the IGS averaged model during September 6, 2017 at 12:00 UTC.

As can be noticed, the spatial pattern extracted from the four different models, within the three geographical strips, coincide with the IGS averaged model, except the JPL model, which gain the same spatial pattern for the middle and high strips, but exhibit a bias from all the other models. As such, we choose to use the low latitude strip, as was also pointed out by Liu *et al.* [60], where all models agree with each other. Thus, we used the unified IGS low latitude strip model for the learning process. After classifying all the relevant solar flare events and their conjugated TEC maps, we ended up with 72 triplet sample TEC maps for the X-class solar flares (i.e., each sample contains 96 TEC maps for 1–3 days prior to the solar flare events), 362 samples for the M-class solar flares, 124 samples for the C-class, and 65 samples for the B-class events.

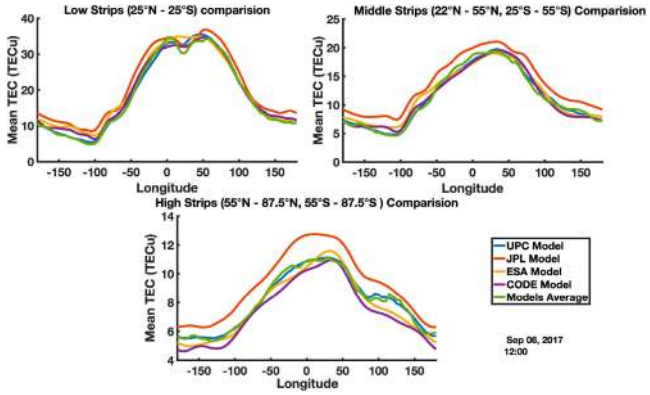

Fig. 5. Comparison between the five different models for extracting global GPS-TEC maps (UPC, CODE, JPL, ESA, and IGS) using low, middle, and high latitude strips mean TEC values from the map resulting on September 6, 2017, 12:00 UTC.

4) TEC Data Rejection Process: As we are aiming to have a pure prediction of solar flares, we filtered out all the relevant maps during days when there were solar disturbances along with high K_p index values ($k_p \geq 6$) or strong earthquakes events (> 6.0 M_w), since several recent studies indicated possible links between earthquakes and the ionospheric F2 layer [61], [62], thus, we ended up with a model that predicts only solar flares and not any other disturbance, which can influence the ionosphere. In addition, we also filtered out days that have more than one flare so we can make sure we are predicting a particular flare and not a day that has several flare events with different magnitudes.

A. TEC Dataset Preprocessing and SVM

After the data retrieval is accomplished, we set to apply several procedures in order to optimize the learning process results. In order to optimize our learning process time, we first deal with feature dimension reduction, applied with the TEC dataset, while taking under consideration how to optimize any loss of information due to the removal of the rows and/or columns from our dataset.

1) Dataset Preprocessing: Daily average maps (AM). In this study, instead of learning the overall $96 \cdot n$ maps for each day, where n is the number of previous days, we estimate an average daily TEC map for each day i. This is an average of 96 overall maps, where each map is a matrix $M_{i,j}$ with a dimension of 73×71 for each day. Thus, the learning process is also applied with one map for each day, allowing us to decrease extensively the amount of data we learn, along with its dimensions to n maps for each studied solar flare event. The data can be represented as a matrix with $73 \times 71 \times n$ elements, which are defined as follows:

$$\text{Avg}_i = \frac{1}{96} \cdot \sum_{j=1}^{96} (M_j). \tag{1}$$

For each day i in year y, the map's matrix is defined as follows:

$$\text{Vec}_{i,y} = \left(\text{Avg}_{1,y}, \text{Avg}_{2,y}, \ldots, \text{Avg}_{n,y}\right). \tag{2}$$

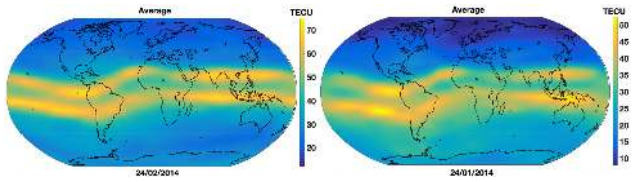

Fig. 6. Example for the AM procedure during quiet (right side) and disturbed (left side) days. During the quiet day (January 24, 2014), TEC values peaks around 50 TECU, where for disturbed days, maximal TEC values peaks above 70 TECU a day before an X-class solar flare event (February 24, 2014) accorded.

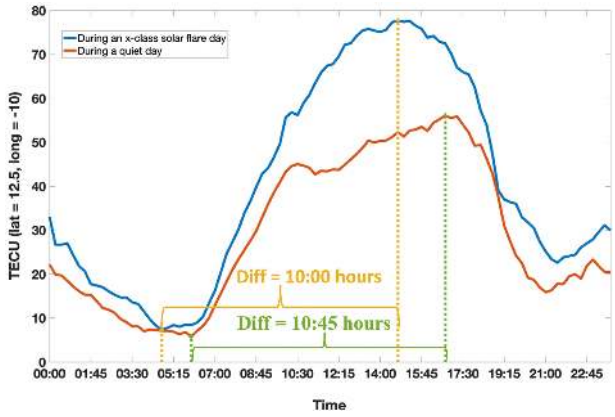

Fig. 7. Comparison between time series of one point (lat $= 12.5$, long $= -10$) during a quiet day (October 5, 2013 - red graph), and a solar-flare day (November 5, 2013 - blue graph).

An example for the resulting procedure is shown in Fig. 6 during quiet and disturbed periods. The AM approach, which averages the 96 maps each day and is mainly (but not entirely) sensitive to the daily variability (which also includes subdaily variations) and shows a smoothed behavior with maximal differences of 0.5–1.5 TECU for the low latitude strips, when an average quite day is compared with a disturbed day.

Subdaily spatial difference trends - Derivative of the maximum difference (DMF). Following the daily AM procedure, for each day we also calculated the derivative (M') of the map difference extracted from the maximum and minimum maps, which takes into account the diurnal (subdaily) variability (at a time scale of half a day, Fig. 7), which is noisier but yield a maximal difference of about 3 TECU for the low latitude strips, when an average quite day is compared with a disturbed day. This procedure can be postulated as

$$\text{Diff}(i,j) = \text{Max}_{i,j} - \text{Min}_{i,j} \tag{3}$$

where Max, Min maps are defined as follows:

$$\text{Max}_{i,j} = \max_{A \in S}(A_{i,j}) \tag{4}$$

$$\text{Min}_{i,j} = \min_{A \in S}(A_{i,j}) \tag{5}$$

where i, j are the latitude, and longitude, respectively, and S is defined as the set of all maps for a given day

$$M'(i,j) = (\text{Diff}(i-1,j) - \text{Diff}(i,j)) + (\text{Diff}(i,j-1) - \text{Diff}(i,j)). \tag{6}$$

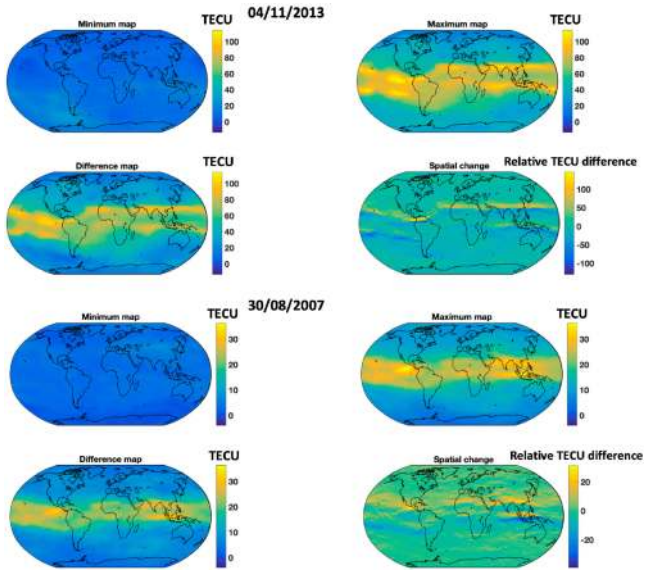

Fig. 8. Examples of the result of the M' matrix during a quiet day (August 31, 2007) (bottom), and one day before an X-class solar flare (November 5, 2013) (up). The resulting maps focus on the local spatial changes inside the map for each day. Strong spatial changes are considered as spatial locally maximal values, unlike the average or differential maps which the strong change is distributed over the entire map.

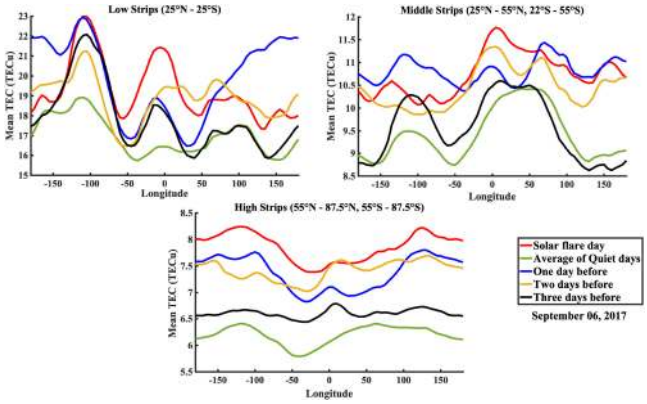

Fig. 9. Low, middle, and high latitude mean strips calculated for AM preprocessing procedure applied on a date that has a solar flare, and the three consecutive days before, as well as on average of quiet days for the same date.

Furthermore, for each day we calculated the DMF between the minimum and maximum maps (see Fig. 8). We then learned the DMF maps of n days before quiet and disturbed days, resulting with n differential maps for each learned event.

2) Data Analysis: Before starting the learning process, it is crucial to verify that there is no loss of information, thus, we first examined the results from both preprocessing approaches (i.e., AM and DMF) by applying them with data during a solar flare (September 6, 2017) event and the three consecutive days before it occurred, along with the average quite day for the same day of year (DOY) averaged from all available maps having no solar flare between the years 1998–2018. As such, we compared the low, middle, and high-latitude mean strips (see Figs. 9 and 10), and verified that there is a significant difference (2.45–7.23 TECU) between the TEC values for the days within the range

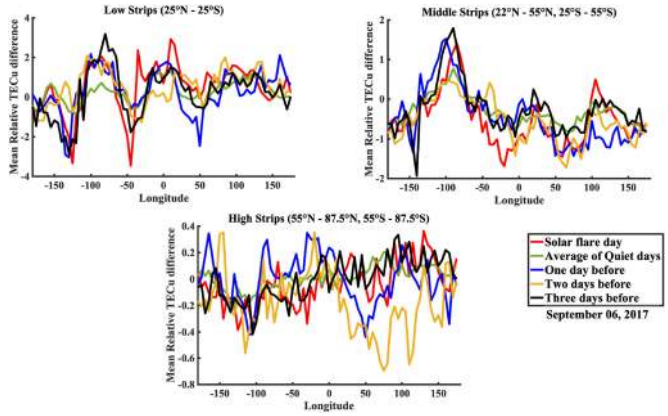

Fig. 10. Low, middle, and high latitude mean strips calculated for DMF preprocessing procedure applied on a date that has a solar flare, and the three consecutive days before, as well as on average of quiet days for the same date.

of the solar flare event (three consecutive days before), and the averaged quiet DOY. This basically means that there are some features we can learn from the database using the suggested approach. In addition, due to the fact that the highest TEC values are found at low latitude strips, but the highest TEC differences between the three consecutive days prior the flare day and the averaged quiet DOY are found at the high latitude strips, it is better to learn the full TEC maps to avoid losing any important information from a particular strip.

3) SVM Technique: A SVM is a supervised machine learning algorithm that can be used for both classification and regression tasks [63]. Given a training set of N data points $\{x_i, y_i\}$, $1 \leq i \leq N$ where $x_i \in R^n$ is the *i*th input pattern (feature vector), n is the data point dimension, and $y_i \in \{+1, -1\}$ is the *i*th output pattern, the SVM builds a hyperplane that is the linear separator, dividing the space into two halfspaces, each of which contains a single sample class. Bestriding the separator are two equidistant parallel planes [64]. The purpose of the SVM is to increase the distance between the linear separator and each of the parallel planes (i.e., the margin). The training examples that are on in direct contact with the parallel planes are called support vectors, hence the name of the technique [65].

The equation representing the separating hyperplane is as follows:

$$w^T x_i + b = 0 \tag{7}$$

where x is the input vector, w is the parameter vector, and b is the bias. As is apparent in Fig. 11, the estimation equation of y_i can be rewritten as follows:

$$\hat{y} = \begin{cases} w^T x_i + b \geq 0, y_i = +1 \\ w^T x_i + b \leq 0, y_i = -1. \end{cases} \tag{8}$$

The support vectors are the vectors closest to the optimized hyperplane, and therefore, are the most difficult to separate, since they are in direct contact with the location of the optimal separation boundary.

a) Hard margin: As we take under consideration the constraints in 8, alternatively, we can write the same that covers

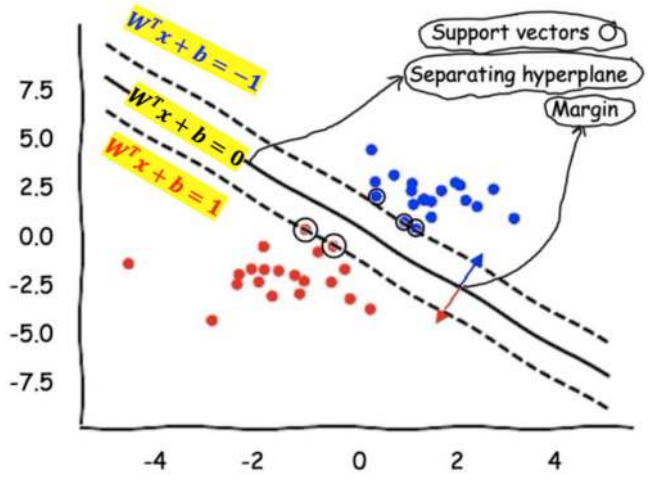

Fig. 11. Illustration for the SVM definitions, with blue dots indicating data points of type 1, and red dots indicating data points of type -1. The blue and red arrows indicate the margin of the hyperplane, and the points surrounded by black circles are the support vectors.

both constraints

$$y_i(w^T x_i + b) \geq 1. \tag{9}$$

In this case, we require that each point should be on the correct side of the hyperplane.

b) Soft margin: SVM can be extended to handle problems where there is no linear separation between the two groups. This is done using the hinge loss function

$$\max(0, 1 - y_i(w^T x_i + b)). \tag{10}$$

The abovementioned function equals zero when the condition required for hard margin is met, i.e., when x_i is on the correct side of the separator. For points that are on the wrong side of the separator, the function receives a value relative to its distance from the separator. Thus, in this approach, we try to minimize the expression

$$\left[\frac{1}{N}\sum_{i=1}^{N}\max(0, 1 - y_i(w^T x_i + b))\right] + \lambda \|W\|^2 \tag{11}$$

where λ defines the extent to which the margin is allowed to expand. For a low λ value the soft margin behaves similarly to the hard margin when the input is linearly separable.

c) Classifier calculation:

1) Primal:
Minimizing 11 can be rewritten as a constrained optimization problem with a differentiable objective function in the following way.
For each $i \in \{1, \ldots, N\}$, we introduce a variable $\zeta_i = \max(0, 1 - y_i(w \cdot x_i + b))$.
We see that ζ_i is the smallest nonnegative number satisfying $y_i(w \cdot x_i + b) \geq 1 - \zeta_i$.
Thus, we can rewrite the optimization problem as follows:

$$\text{minimize} \frac{1}{N}\sum_{i=1}^{N}\zeta_i + \lambda \|W\|^2$$

subject to $y_i(w \cdot x_i + b) \geq 1 - \zeta_i$ and $\zeta_i \geq 0$ for all i. This is called the primal problem.

2) Dual:
By solving for the Lagrangian dual of the abovementioned problem, one obtains the simplified problem

$$\text{maximize} f(c_1 \ldots c_N) = \sum_{i=1}^{N} c_i - \frac{1}{2}\sum_{i=1}^{N}\sum_{j=1}^{N} y_i c_i (x_i \cdot x_j) y_i c_j$$

$$\text{subject to } \sum_{i=1}^{N} c_i y_i = 0, \text{ and } 0 \leq c_i \leq \frac{1}{2n\lambda} \text{ for all } i.$$

Here, the variables c_i are defined such that

$$\vec{w} = \sum_{i=1}^{N} y_i c_i \vec{x_i}.$$

Moreover, $c_i = 0$ exactly when $\vec{x}_i$ lies on the correct side of the margin, and $0 < c_i < (2n\lambda)^{-1}$ when $\vec{x}_i$ lies on the margin's boundary. It follows that $\vec{w}$ can be written as a linear combination of the support vectors. The offset b can be recovered by finding an $\vec{x}_i$ on the margin's boundary and solving

$$y_i(\vec{w} \cdot \vec{x}_i - b) = 1 \iff b = \vec{w} \cdot \vec{x}_i - y_i.$$

3) Nonlinear separation using the kernel trick:
The idea in this approach is to embed the training examples from the original linear space to a higher dimension space, with the hope we can find a better linear separator that in the new space. Embedding is done using the kernel trick, by replacing the inner product used for the linear separator with a kernel function that simulates the redistribution of the original vectors in a richer space, without significant computational cost. However, the transition to a higher dimension may result in an increase in the generalization error. The linear separator in the new vector space corresponds to a nonlinear separator in the original space. The classification work is also performed with the help of the nuclear operator. Then, the SVM method aims to construct a classifier of the form

$$\text{SVM}(x) = \text{sign}\left[\sum_{k=1}^{N}\alpha_k y_k \psi(x, x_k) + b\right] \tag{12}$$

where α_k are positive real constants and b is bias, and $\psi(x, x_k)$ is the kernel function. Here, we consider several functions for $\psi(x, x_k)$. One typically has the following choices:

1) linear SVM: $\psi(x, x_k) = x_k^T x$;
2) polynomial SVM of degree d : $\psi(x, x_k) = (x_k^T x + 1)^d$;
3) radial basis function (RBF SVM): $\psi(x, x_k) = e^{\frac{-\|x - x_k\|^2}{\sigma^2}}$;

4) two layer (TL SVM) neural network: $\psi(x, x_k) = \tanh kx_k^T + \theta$.

Where σ, k, θ are parameters that are tuned during the learning process.

Each input map is flattened to a vector by concatenating its rows into a single vector. For each solar flares class (X, M, C, and B-class), we separately trained each of the abovementioned four SVM models of different kernels. Moreover, each model was trained on two different type of inputs, AM and DMF TEC maps, in order to predict whether a flare will occur within 0, 1, 2, or 3 days ahead, where 0 implies that no flare event will occur at all. The SVM algorithm utilized in our study was implemented using MATLAB environment.[1]

IV. Experimental Results

A. Data Splitting

Applying ML approaches to a given set of measurements typically requires splitting the data into two sets: Training-set: which consists all the data that the model will be trained on, and testing set (an unseen Test-set): which consists of the data that the resulting model will be tested on after the training process is been finished. A common separation ratio which we used in this study was set to 70% and 30% for the training and test sets, respectively. Due to the fact that the available solar flare data might not be sufficient to train our model, allocating part of it for the test-set could pose an issue of underfitting. Thus, by reducing the amount of the training dataset, we risk losing important patterns and features, which can increase the overall error induced by the bias. Therefore, in order to overcome this issue, we used the $k-$fold cross validation technique [66], which provide sufficient amount of data for training the model while also leaving enough data for validation (i.e., the test-set). $k-$fold cross validation technique divides the training set into k subsets, while for each repetition one of the k subsets is used as a test set and the remaining $k-1$ subsets are assembled to form the training set. The process repeats itself k times, and the error estimation is averaged over all k repetitions to achieve optimal effectiveness of the model. the k value used in the current study was set to 10% of the training sets.

B. Results

Given the results, it is necessary to characterize the performance. A useful way is by using different combinations between TP, FN, TN, and FP to express different aspects of the model performance and output quality

$$\text{Precision} = \frac{\text{TP}}{\text{TP}+\text{FP}} \tag{13}$$

$$\text{Recall} = \frac{\text{TP}}{\text{TP}+\text{FN}} \tag{14}$$

$$\text{HSS} = \frac{2\cdot[(\text{TP}\times\text{TN})-(\text{FN}\times\text{FP})]}{(\text{TP}+\text{FN})\cdot(\text{FN}+\text{TN})+(\text{TP}+\text{FN})\cdot(\text{FP}+\text{TN})} \tag{15}$$

[1][Online]. Available: https://www.mathworks.com/discovery/support-vector-machine.html SVM Matlab

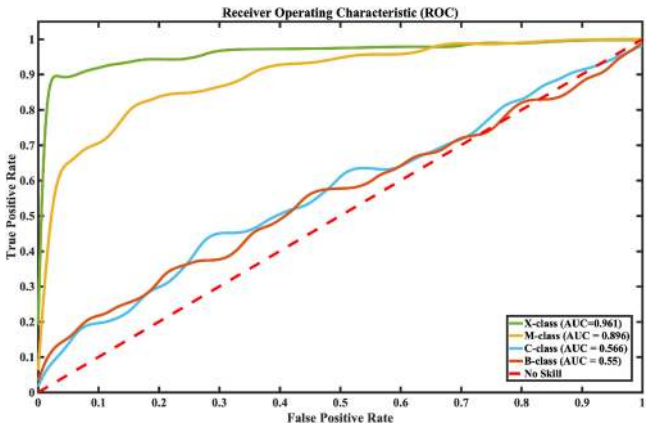

Fig. 12. Comparison of ROC curves for the best performance obtained when the two classes are X/M/C/B-class solar flares and no event occurrence, applying the TL SVM and DMF products. C, and B predictors have very poor predictive power (AUC ~ 0.56 - asymptotically behaves as the "no skill" line) as it cannot differentiate between a solar flare and nonsolar flare days, while X and M predictors have the ability for highly accurate prediction of a solar flares (AUC ~ 0.96 and AUC ~ 0.89, respectively).

$$\text{Accuracy} = \frac{\text{TP}+\text{TN}}{\text{P}+\text{N}} \tag{16}$$

$$\text{TSS} = \frac{\text{TP}}{\text{TP}+\text{FN}} - \frac{\text{FP}}{\text{FP}+\text{TN}}. \tag{17}$$

While the precision term aims to quantify the fraction of relevant instances (true positive identifications) among the retrieved instances (true positive plus false positive identifications), the recall term (also known as the sensitivity term) aims to quantity the fraction of the total amount of relevant instances (true positive identifications) that were actually retrieved (from the true positive plus false negative identification). The accuracy term (ACC) aims to quantify how well a classification test correctly identifies or excludes a condition (i.e., whether it's a TP or TN). The Heidke skill score (HSS) [67] aims to quantify the fractional improvement of the prediction accuracy relative to some set of control or reference predictions. It is normalized by the total range of possible improvement over the standard (which basically means it can be compared with different datasets). The range of the HSS is defined as: HSS $= 1$ is a perfect prediction; HSS $= 0$ shows no skill. If HSS < 0, the prediction is worse than the reference prediction. The true skill statistics (TSS) [68] term on the other hand compares the probability of the true prediction, to the probability of false prediction. The range of the TSS is between -1 and +1, where the value 0 means that the algorithm has no effect. High positive values indicate that the algorithm performs well, while negative values indicate a contradictory behavior, suggesting that the labels should be reversed. Another widely used performance measurement tool is the receiver operating characteristics (ROC) curve (see Fig. 12), which give us a sense of how much the model is capable of distinguishing between classes at all classification thresholds. Higher area under curve (AUC) values mean that the model performs better at predicting flare/nonflare days. The AUC term summarizes the integral (i.e., the area under the ROC curve). The results of the 4 different SVM ψ kernel functions described in

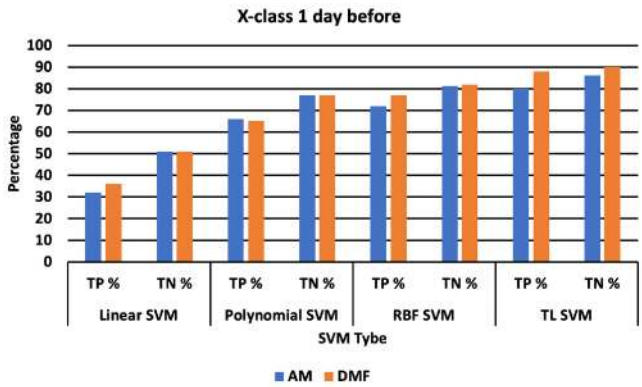

(a)

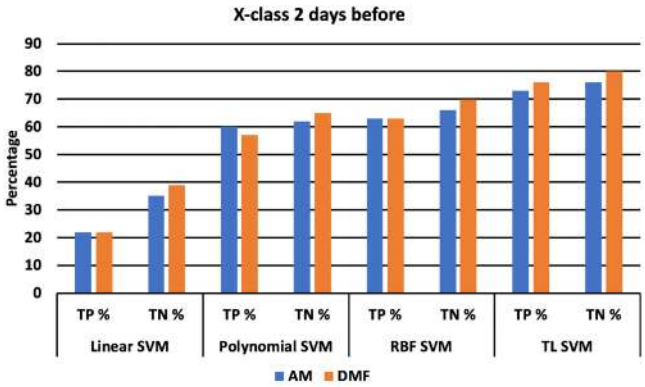

(b)

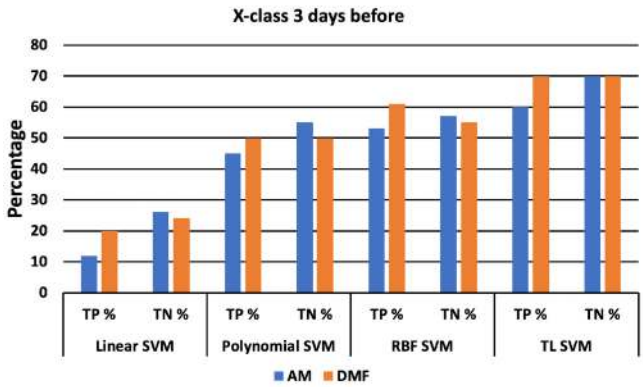

(c)

Fig. 13. X class prediction results by applying the 4 different ψ SVM kernel functions on both AM and DMF proposed methods for one (a), two (b), and three (c) days before the solar flare events.

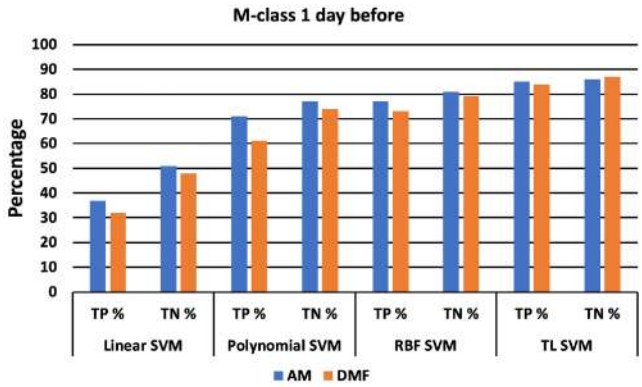

(a)

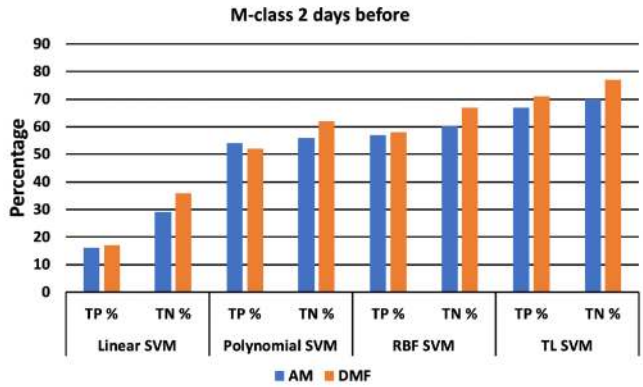

(b)

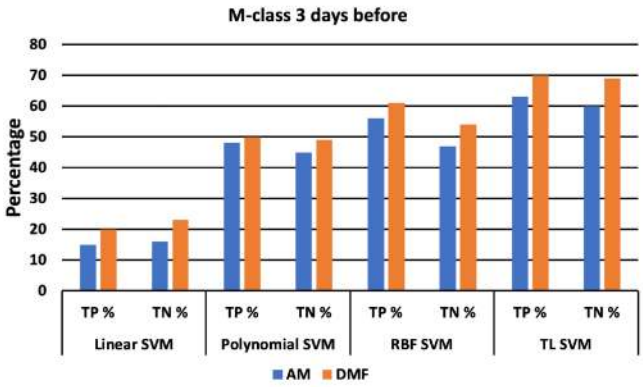

(c)

Fig. 14. M class prediction results by applying the 4 different ψ SVM kernel functions on both AM and DMF proposed methods for one (a), two (b), and three (c) days before the solar flare events.

Section III-E3 applied on the two proposed methods described in Sections III-E1 and III-E1 with 1, 2, and 3 days before the solar flare events are shown in Figs. 13– 16 for X, M, C, and B class solar flares, respectively.

V. Discussion

In this study, we propose a new methodology for predicting solar flare events, up to 3 days before they occur, by applying SVM technique with TEC maps extracted from GPS ionospheric path delays. Two approaches for learning the data were developed: The AM and the DMF. Considering the number of days before a solar flare event occurs, the AM approach reduces the input dimensions by a factor of 96 when taking the average map of each of the n days instead of taking 96 maps for each day and learning them. The DMF approach aims to learn the spatial change of each day by taking the derivative of the map, which was produced

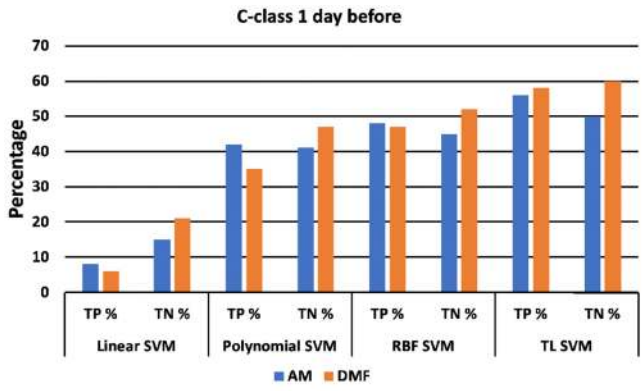

(a)

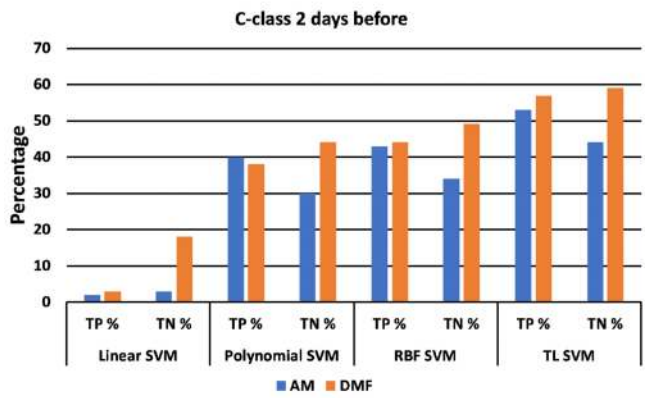

(b)

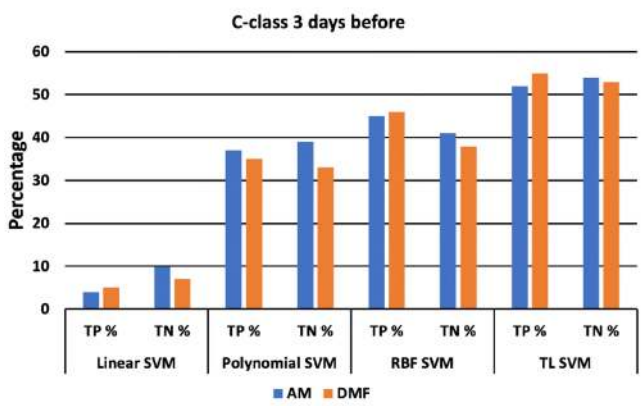

(c)

Fig. 15. C class prediction results by applying the 4 different ψ SVM kernel functions on both AM and DMF proposed methods for one (a), two (b), and three (c) days before the solar flare events.

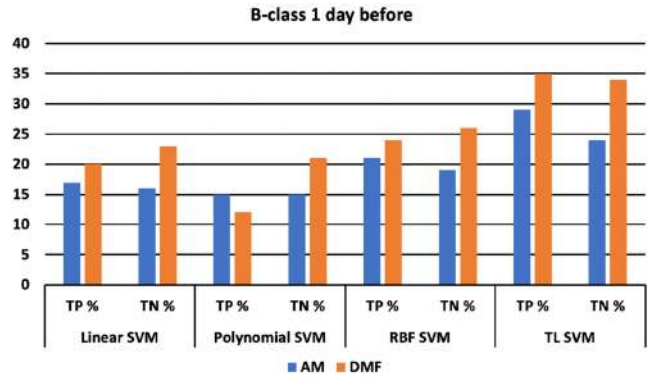

(a)

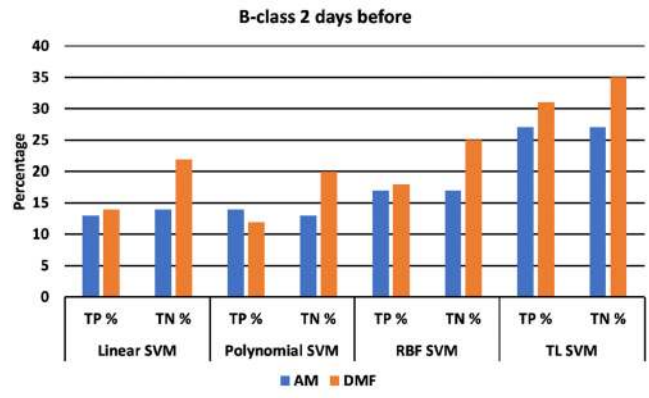

(b)

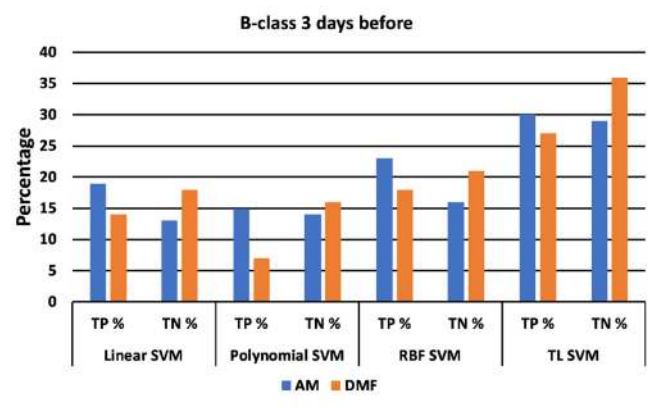

(c)

Fig. 16. B class prediction results by applying the 4 different ψ SVM kernel functions on both AM and DMF proposed methods for one (a), two (b), and three (c) days before the solar flare events.

from the elementwise maximum difference for each day, while learning these $3 \cdot n$ maps. As a preprocessing step. We tested 4 different variations of kernel functions for the SVM in order to learn the AM and DMF products. The results indicate that the best combination is achieved by learning the spatial changes (the DMF approach), using two-layer neural network SVM with the $\tanh(kk_x^T + \theta)$ as the kernel function, which results in the prediction of solar flare events of the X and M-classes with 80%–90% and 80%–87% accuracy, for $n \in [1, 3]$, respectively. The results also indicate that the proposed method does not succeed in predicting small-size C- and B-class solar flares. This outcome can be rationalized by the fact that small-size flares have small impact on the ionization effects in the ionosphere, explained leaving the TEC unchanged.

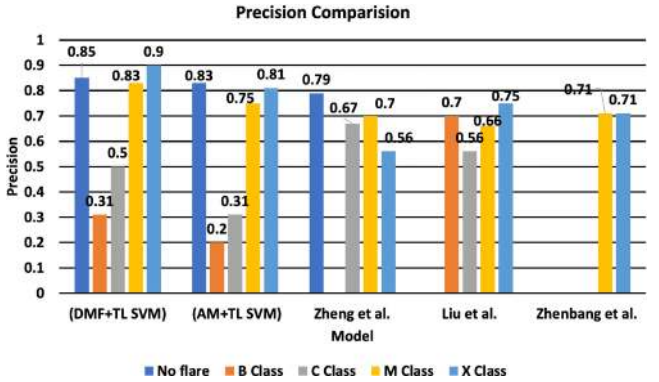

Fig. 17. Multiclass solar flare prediction results within 24 h of our methods (DMF/AM) with TL SVM in comparison with previous methods using precision metric.

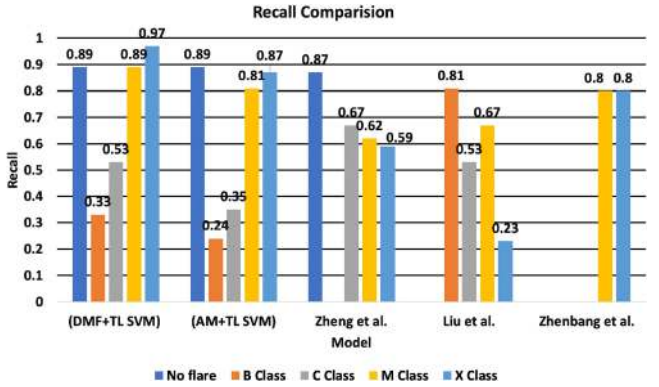

Fig. 18. Multiclass solar flare prediction results within 24h of our methods (DMF/AM) with TL SVM in comparison with previous methods using recall metric.

After sorting all the solar flares dates that are relevant to the TEC maps we have, we were left with a relatively small amount of data that the algorithm could be taught, which could be one of the reasons why the algorithm does not perform well on small-size solar flares (in addition to their insufficient power). The average behavior of the cost function across iterations decreased exponentially, but relatively slowly due to the fact that the learning rate of the gradient decent algorithm was 10^{-3} in order to try to achieve the best results.

The best results we achieved (1 d before each Solar flare) using both methods (DMF and AM), while trained by a TL SVM, are compared with the abovementioned previous studies in Figs. 17–21. The proposed methodology presented previously achieves better results in comparison with most previous related works; 12%–15% improvement for the precision skill scores, 9%–17% improvement for the recall skill scores, 21%–37% improvements for the HSS skill scores, 1%–2% improvement for the Accuracy skill scores, and 11%–24% improvement for the TSS skill scores, for X, and M class solar flare predictions, respectively. However, for the small size solar flares (B, C classes), the suggested approach does not succeed in producing similar promising results. Furthermore, all previous studies used X-ray time series, sunspots data, and active region analysis, which required using image processing-based ML techniques

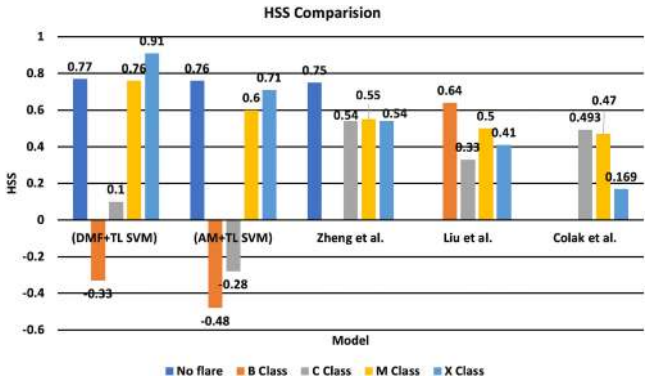

Fig. 19. Multiclass solar flare prediction results within 24 h of our methods (DMF/AM) with TL SVM in comparison with previous methods using HSS metric.

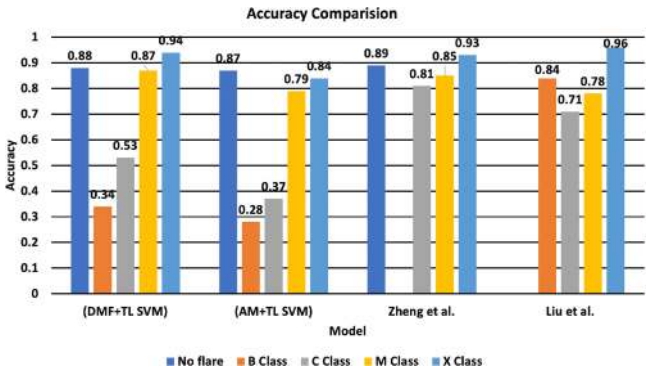

Fig. 20. Multiclass solar flare prediction results within 24 h of our methods (DMF/AM) with TL SVM in comparison with previous methods using accuracy metric.

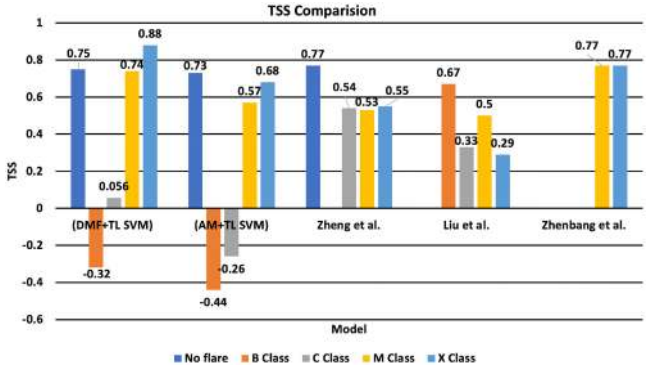

Fig. 21. Multiclass solar flare prediction results within 24 h of our methods (DMF/AM) with TL SVM in comparison with previous methods using TSS metric.

or more complex ML models, which concededly consume more time and computing power. Here, we suggest using the SVM algorithm in order to classify spatial changes within global TEC maps to predict whether there will be a solar flare events up to three days ahead.

VI. Conclusion

We present the use of SVM applied with ionospheric TEC data, derived from worldwide GPS geodetic receiver network,

in order to evaluate the possibility of predicting B, C, M, and X-class solar flare events. While testing a wide range of possible products estimated from the initial GPS-TEC maps, taking into account low data budget, we conclude that when using the DMF variation applied with TL-SVM technique, the model has the ability to predict solar flare events of X and M-class with 91% and 76% HSS skill score, respectively. However, the proposed method does not succeed with small-size solar flares, such as B and C, where the HSS skill score decreases to −0.3%–0.1%. This can be attributed to the difficulty in obtaining sufficient amount of TEC samples to train the SVM classifier with small-size solar flare events, along with the fact these small sized bursts have negligible impact on the ionosphere. Future work might include a modified combination of TEC measurements and additional remote sensing data, which will better preserve small-sized features related to the flare events that could not be identified through TEC modifications. This might also improve the accuracy of small-size solar flare predictions.

SOURCE CODE

The source code of the preprocessing steps as well as the best model parameters can be found at:

https://github.com/saedAsa/TEC_SolarFlare.git

AUTHOR CONTRIBUTIONS

All authors have made significant contributions to the manuscript. Saed Asaly processed the GPS-TEC data along with the solar flare data, designed, and implemented the SVM algorithms development, wrote the main manuscript text and prepared all the figures and tables in the manuscript; Lee-Ad Gottlieb revised the manuscript; Yuval Reuveni conceived and designed part of the algorithm development, analyzed the data and results and is the main author who developed and revised the manuscript.

REFERENCES

[1] D. N. Baker, "Satellite anomalies due to space storms," in *Space Storms and Space Weather Hazards*. New York, NY, USA: Springer, 2001, pp. 285–311.

[2] R. Turner, "Solar particle events from a risk management perspective," *IEEE Trans. Plasma Sci.*, vol. 28, no. 6, pp. 2103–2113, Dec. 2000.

[3] J. M. Goodman, *Space Weather & Telecommunications*, vol. 782. New York, NY, USA: Springer, 2006.

[4] M. A. Clilverd *et al.*, "Remote sensing space weather events: Antarctic-arctic radiation-belt (dynamic) deposition-VLF atmospheric research konsortium network," *Space Weather*, vol. 7, no. 4, pp. 1–15, 2009.

[5] G. Tóth *et al.*, "Space weather modeling framework: A new tool for the space science community," *J. Geophysical Res., Space Phys.*, vol. 110, no. A12, 2005, Art. no. A12226.

[6] H. Koizumi, R. Noji, K. Komurasaki, and Y. Arakawa, "Plasma acceleration processes in an ablative pulsed plasma thruster," *Phys. Plasmas*, vol. 14, no. 3, 2007, Art. no. 033506.

[7] M. Lyutikov, S. Komissarov, L. Sironi, and O. Porth, "Particle acceleration in explosive relativistic reconnection events and crab nebula gamma-ray flares," *J. Plasma Phys.*, vol. 84, no. 2, 2018, Art. no. 635840201. [Online]. Available: https://www.cambridge.org/core/journals/journal-of-plasma-physics/article/particle-acceleration-in-explosive-relativistic-reconnection-events-and-crab-nebula-gammaray-flares/87EF424B9DFC5B775CE4FCBABA70729C

[8] T. Nagem, R. Qahwaji, S. Ipson, and A. Alasta, "Predicting solar flares by converting goes x-ray data to gramian angular fields (GAF) images," in *Proc. World Congr. Eng.*, vol. 1, 2018. [Online]. Available: https://www.semanticscholar.org/paper/Predicting-Solar-Flares-by-Converting-GOES-X-ray-to-Nagem-Qahwaji/ec61a4d82651c6577d0bc81d4548a45caa19989a

[9] C. F. Baggett, E. A. Barnes, E. D. Maloney, and B. D. Mundhenk, "Advancing atmospheric river forecasts into subseasonal-to-seasonal time scales," *Geophysical Res. Lett.*, vol. 44, no. 14, pp. 7528–7536, 2017.

[10] I. Zhelavskaya, R. Vasile, Y. Shprits, C. Stolle, and J. Matzka, "Systematic analysis of machine learning and feature selection techniques for prediction of the Kp index," *Space Weather*, vol. 17, no. 10, pp. 1461–1486, 2019.

[11] G. Balasis, S. Aminalragia-Giamini, C. Papadimitriou, I. A. Daglis, A. Anastasiadis, and R. Haagmans, "A machine learning approach for automated ULF wave recognition," *J. Space Weather Space Climate*, vol. 9, pp. 1–11, 2019.

[12] A. Smirnov *et al.*, "Medium energy electron flux in Earth's outer radiation belt (MERLIN): A machine learning model," *Space Weather*, vol. 18, 2020, Art. no. e2020SW002532.

[13] J. Liu, C.-H. Lin, H. Tsai, and Y. Liou, "Ionospheric solar flare effects monitored by the ground-based GPS receivers: Theory and observation," *J. Geophysical Res., Space Phys.*, vol. 109, no. A1, 2004, Art. no. A01307.

[14] P. A. Sweet, "14. the neutral point theory of solar flares," in *Proc. Symp.-Int. Astron. Union*, vol. 6, pp. 123–134, 1958.

[15] R. R. Freeman, J. A. King, and G. P. Lafyatis, *Electromagnetic Radiation*. London, U.K.: Oxford Univ. Press, 2019.

[16] B. Kong, E. Wang, and Z. Li, "The effect of high temperature environment on rock properties-an example of electromagnetic radiation characterization," *Environ. Sci. Pollut. Res.*, vol. 25, no. 29, pp. 29 104–29 114, 2018.

[17] A. Papaioannou *et al.*, "Solar flares, coronal mass ejections and solar energetic particle event characteristics," *J. Space Weather Space Climate*, vol. 6, pp. 1–29, 2016.

[18] D. Baker, E. Daly, I. Daglis, J. G. Kappenman, and M. Panasyuk, "Effects of space weather on technology infrastructure," *Space Weather*, vol. 2, no. 2, 2004. [Online]. Available: https://agupubs.onlinelibrary.wiley.com/doi/full/10.1029/2003SW000044

[19] H. Jung, K. Taniguchi, and C. Hamaguchi, "Impact ionization model for full band monte carlo simulation in gaas," *J. Appl. Phys.*, vol. 79, no. 5, pp. 2473–2480, 1996.

[20] Y. Cui, R. Li, L. Zhang, Y. He, and H. Wang, "Correlation between solar flare productivity and photospheric magnetic field properties," *Sol. Phys.*, vol. 237, no. 1, pp. 45–59, 2006.

[21] L. Qian, W. Wang, A. Burns, P. Chamberlin, and A. Coster, "Concurrent solar flare and geomagnetic storm effects on the thermosphere and ionosphere during september 2017," in *Proc. AGU Fall Meet. Abstr.*, 2018, pp. L105–L108.

[22] A. Kosovichev and V. Zharkova, "Magnetic energy release and transients in the solar flare of 2000 July 14," *Astrophysical J. Lett.*, vol. 550, no. 1, pp. L105–L108, 2001.

[23] M. Lockwood, S. Cowley, P. Sandholt, and R. Lepping, "The ionospheric signatures of flux transfer events and solar wind dynamic pressure changes," *J. Geophysical Res., Space Phys.*, vol. 95, no. A10, pp. 17 113–17 135, 1990.

[24] Y. Zheng, X. Li, and X. Wang, "Solar flare prediction with the hybrid deep convolutional neural network," *Astrophysical J.*, vol. 885, no. 1, pp. 73–86, 2019.

[25] C. Liu, N. Deng, J. T. Wang, and H. Wang, "Predicting solar flares using SDO/HMI vector magnetic data products and the random forest algorithm," *Astrophysical J.*, vol. 843, no. 2, pp. 104–117, 2017.

[26] T. Colak and R. Qahwaji, "Automated solar activity prediction: A hybrid computer platform using machine learning and solar imaging for automated prediction of solar flares," *Space Weather*, vol. 7, no. 6, pp. 1–12, 2009.

[27] Z. Jiao *et al.*, "Solar flare intensity prediction with machine learning models," *Space Weather*, vol. 18, no. 7, 2020, Art. no. e2020SW002440.

[28] F. Arikan, S. Shukurov, H. Tuna, O. Arikan, and T. Gulyaeva, "Performance of GPS slant total electron content and IRI-plas-STEC for days with ionospheric disturbance," *Geodesy Geodynamics*, vol. 7, no. 1, pp. 1–10, 2016, Art. no. S06001.

[29] J. K. Hargreaves, *The Solar-Terrestrial Environment: An Introduction to Geospace-the Science of the Terrestrial Upper Atmosphere, Ionosphere, and Magnetosphere*. Cambridge, U.K.: Cambridge University Press, 1992.

[30] Y. Reuveni and C. Price, "A new approach for monitoring the 27-day solar rotation using VLF radio signals on the Earth's surface," *J. Geophysical Res.*, vol. 114, Oct. 2009, Art. no. A10306.
[31] Y. Reuveni, C. Price, E. Greenberg, and A. Shuval, "Natural atmospheric noise statistics from VLF measurements in the eastern Mediterranean," *Radio Sci.*, vol. 45, no. 5, pp. 1–9, 2010.
[32] A. Krankowski, W. Kosek, L. Baran, and W. Popinski, "Wavelet analysis and forecasting of VTEC obtained with GPS observations over European latitudes," *J. Atmospheric Solar-Terr. phys.*, vol. 67, no. 12, pp. 1147–1156, 2005.
[33] N. Jakowski, S. Heise, A. Wehrenpfennig, S. Schlüter, and R. Reimer, "GPS/glonass-based TEC measurements as a contributor for space weather forecast," *J. Atmospheric Solar-Terr. Phys.*, vol. 64, no. 5/6, pp. 729–735, 2002.
[34] Y. Reuveni, Y. Bock, X. Tong, and A. W. Moore, "Calibrating interferometric synthetic aperture radar (INSAR) images with regional GPS network atmosphere models," *Geophysical J. Int.*, vol. 202, no. 3, pp. 2106–2119, 2015.
[35] E. Erdogan, M. Schmidt, F. Seitz, and M. Durmaz, "Near real-time estimation of ionosphere vertical total electron content from GNSS satellites using B-splines in a kalman filter," in *Proc. Annales Geophysicae*, 2017, vol. 35, pp. 263–277.
[36] E. Thomas, J. Baker, J. Ruohoniemi, A. Coster, and S.-R. Zhang, "The geomagnetic storm time response of GPS total electron content in the north american sector," *J. Geophysical Res., Space Phys.*, vol. 121, no. 2, pp. 1744–1759, 2016.
[37] B. Zhang, "Three methods to retrieve slant total electron content measurements from ground-based GPS receivers and performance assessment," *Radio Sci.*, vol. 51, no. 7, pp. 972–988, 2016.
[38] A. Van Dierendonck, Q. Hua, P. Fenton, and J. Klobuchar, "Commercial ionospheric scintillation monitoring receiver development and test results," *52nd Annu. Meeting Inst. Navigation*, 1996, pp. 573–582.
[39] W. Sun *et al.*, "Forecasting of ionospheric vertical total electron content (TEC) using LSTM networks," in *Proc. Int. Conf. Mach. Learn. Cybern.*, 2017, vol. 2, pp. 340–344.
[40] L. Liu, S. Zou, Y. Yao, and Z. Wang, "Forecasting global ionospheric total electron content (TEC) using deep learning approach," *Space Weather*, vol. 18, 2020, Art. no. e2020SW002501.
[41] A. D. Hands, K. A. Ryden, N. P. Meredith, S. A. Glauert, and R. B. Horne, "Radiation effects on satellites during extreme space weather events," *Space Weather*, vol. 16, no. 9, pp. 1216–1226, 2018.
[42] U. C. Benz, P. Hofmann, G. Willhauck, I. Lingenfelder, and M. Heynen, "Multi-resolution, object-oriented fuzzy analysis of remote sensing data for GIS-ready information," *ISPRS J. Photogrammetry Remote Sens.*, vol. 58, no. 3/4, pp. 239–258, 2004.
[43] J. Zhang, "Multi-source remote sensing data fusion: Status and trends," *Int. J. Image Data Fusion*, vol. 1, no. 1, pp. 5–24, 2010.
[44] H. Mavromichalaki *et al.*, "Space weather prediction by cosmic rays," *Adv. Space Res.*, vol. 37, no. 6, pp. 1141–1147, 2006.
[45] V. Barrile, M. Cacciola, F. C. Morabito, and M. Versaci, "TEC measurements through GPS and artificial intelligence," *J. Electromagn. Waves Appl.*, vol. 20, no. 9, pp. 1211–1220, 2006.
[46] Z. Liu and C. J. Sullivan, "Prediction of weather induced background radiation fluctuation with recurrent neural networks," *Radiat. Phys. Chem.*, vol. 155, pp. 275–280, 2019.
[47] M. B. Terzi, O. Arikan, S. Karatay, F. Arikan, and T. Gulyaeva, "Classification of regional ionospheric disturbance based on machine learning techniques," *Eur. Space Agency*, vol. 740, 2016, Art. no. 279.
[48] M. Hostetter, A. Ahmadzadeh, B. Aydin, M. K. Georgoulis, D. J. Kempton, and R. A. Angryk, "Understanding the impact of statistical time series features for flare prediction analysis," in *Proc. IEEE Int. Conf. Big Data*, 2019, pp. 4960–4966.
[49] H. Lan, H. Yin, Y.-Y. Hong, S. Wen, C. Y. David, and P. Cheng, "Day-ahead spatio-temporal forecasting of solar irradiation along a navigation route," *Appl. Energy*, vol. 211, pp. 15–27, 2018.
[50] L. Duc, K. Saito, and H. Seko, "Spatial-temporal fractions verification for high-resolution ensemble forecasts," *Tellus A, Dyn. Meteorol. Oceanogr.*, vol. 65, no. 1, 2013, Art. no. 18171.
[51] G. L. Perry and M. E. Dickson, "Using machine learning to predict geomorphic disturbance: The effects of sample size, sample prevalence, and sampling strategy," *J. Geophysical Res., Earth Surf.*, vol. 123, no. 11, pp. 2954–2970, 2018.
[52] T. Kavzoglu, I. Colkesen, and E. K. Sahin, "Machine learning techniques in landslide susceptibility mapping: A survey and a case study," in *Landslides: Theory, Pract. Modelling*. New York, NY, USA: Springer, 2019, pp. 283–301.
[53] C. Cortes, L. D. Jackel, and W.-P. Chiang, "Limits on learning machine accuracy imposed by data quality," in *Proc. Adv. Neural Inf. Process. Syst.*, 1995, pp. 239–246.
[54] G. C. Cawley and N. L. Talbot, "Preventing over-fitting during model selection via Bayesian regularisation of the hyper-parameters," *J. Mach. Learn. Res.*, vol. 8, pp. 841–861, 2007.
[55] N. K. Ahmed, A. F. Atiya, N. E. Gayar, and H. El-Shishiny, "An empirical comparison of machine learning models for time series forecasting," *Econometric Rev.*, vol. 29, no. 5/6, pp. 594–621, 2010.
[56] S. Suthaharan, "Machine learning models and algorithms for big data classification," *Integr. Ser. Inf. Syst*, vol. 36, pp. 1–12, 2016.
[57] J. Wang and L. Perez, "The effectiveness of data augmentation in image classification using deep learning," *Convolutional Neural Netw. Vis. Recognit.*, vol. 11, pp.1–8, 2017.
[58] J.-P. Zuo, Y. Zhao, N.-B. Chai, and H.-W. Wang, "Measuring micro/meso deformation field of GEO-materials with SEM and digital image correlation method," *Adv. Sci. Lett.*, vol. 4, no. 4/5, pp. 1556–1560, 2011.
[59] M. Hernández-Pajares *et al.*, "The IGS VTEC maps: A reliable source of ionospheric information since 1998," *J. Geodesy*, vol. 83, no. 3/4, pp. 263–275, 2009.
[60] L. Liu, W. Wan, B. Ning, and M.-L. Zhang, "Climatology of the mean total electron content derived from GPS global ionospheric maps," *J. Geophysical Res., Space Phys.*, vol. 114, no. A6, 2009, Art. no. A06308.
[61] E. L. Afraimovich and E. I. Astafyeva, "TEC anomalies-local TEC changes prior to earthquakes or TEC response to solar and geomagnetic activity changes?," *Earth, Planets Space*, vol. 60, no. 9, pp. 961–966, 2008.
[62] N. Ya'acob, M. Ismail, and M. Abdullah, "Investigation of the GPS signals ionospheric correction: Ionospheric TEC prediction over equatorial," in *Proc. IEEE Int. Conf. Telecommun. Malaysia Int. Conf. Commun.*, 2007, pp. 294–298.
[63] J. A. Suykens and J. Vandewalle, "Least squares support vector machine classifiers," *Neural Process. Lett.*, vol. 9, no. 3, pp. 293–300, 1999.
[64] G. Cauwenberghs and T. Poggio, "Incremental and decremental support vector machine learning," in *Proc. Adv. Neural Inf. Process. Syst.*, 2001, pp. 409–415.
[65] W. S. Noble, "What is a support vector machine?," *Nat. Biotechnol.*, vol. 24, no. 12, pp. 1565–1567, 2006.
[66] J. D. Rodriguez, A. Perez, and J. A. Lozano, "Sensitivity analysis of k-fold cross validation in prediction error estimation," *IEEE Trans. Pattern Anal. Mach. Intell.*, vol. 32, no. 3, pp. 569–575, Mar. 2010.
[67] P. Heidke, "Calculation of the success and the quality of the wind force forecasts in the storm warning service," (in German), *Geografiska Annaler*, vol. 8, no. 4, pp. 301–349, 1926.
[68] A. Hanssen and W. Kuipers, *On the Relationship Between the Freq. of Rain and Various Meteorol. Parameters: (with Reference to the Problem of Objective Forecasting).* De Bilt, The Netherlands: Koninklijk Nederlands Meteorologisch Instituut, 1965.

Saed Asaly received the B.Sc. and M.Sc. degrees in computer science and mathematics from Ariel University, Ariel, israel, in 2014 and 2018, respectively, where he is currently working toward the Ph.D. degree in computer science.

His research interests include applying and developing machine learning and deep learning techniques with remote sensing data, in order to predict natural hazards.

Lee-Ad Gottlieb received the B.Sc. degree in applied math and computer science from Brown University, Providence, RI, USA, in 2002, and the M.Sc. and Ph.D. degrees in computer science from the Courant Institute of Mathematical Science, New York University, New York, NY, USA, 2006 and 2009, respectively.

He was with the Department of Computer Science, Ariel University, in 2012. His research interests include proximity problems in metric space, with emphasis on problems in machine learning, computational geometry, and metric embeddings.

Yuval Reuveni received the B.Sc., M.Sc., and Ph.D. degrees in geophysics, atmospheric and space sciences from Tel-Aviv University, Tel Aviv, Israel, in 2002, 2005, and 2011, respectively.

He was with the Eastern R&D center as the Head of the Department of Geophysics and Space Sciences, in 2015, and the Physics Department, Ariel University, in 2017. His research interests include combining various data analysis techniques and remote sensing measurements from ground and space-based instruments, to study electromagnetic wave propagation, ionospheric physics, space weather, and space geodesy phenomena.